E. B. Svendsen[1], L. Nielsen[1], B. Nilsson[2], K. H. Kjær[3], and M. C. Looms[1]

[1] Department of Geosciences and Natural Resource Management, University of Copenhagen, Denmark.

[2] Geological Survey of Denmark and Greenland (GEUS), Denmark.

[3] Globe Institute, University of Copenhagen, Denmark.

Corresponding author: Espen Bing Svendsen (esbs@ign.ku.dk)

Key Points:

- Crosshole ground-penetrating radar can provide valuable information about clay-rich media on the decimeter- to meter-scale.
- Radar wave amplitude and shape attributes are more sensitive to changes in material properties than radar velocity is.
- We present a shortlist of four robust attributes (out of 43 tested) that provide different information about clay-rich materials.

Abstract

Knowing the centimeter- to meter-scale distribution of sand in clayey deposits is important for determining the dominating water flow pathways. Borehole information has a high vertical resolution, on the millimeter- to centimeter-scale, but provides poor lateral coverage. For highly heterogeneous deposits, such as glacial diamicts, this detailed borehole information may not be sufficient for creating reliable geological models. Crosshole ground-penetrating radar (GPR) can provide information on the decimeter- to meter-scale variation between boreholes, as the GPR response depends on the dielectric permittivity, electric conductivity, and the magnetic permeability of the subsurface. In this study, we investigate whether crosshole GPR can provide information on the material properties of diamicts, such as water content, bulk density, and clay content, as well as their structural relationships. To achieve ground truth, we compare the crosshole GPR data with geological information from both boreholes and excavation at the field site. The GPR data were analyzed comprehensively using several radar wave attributes in both time- and frequency domain, describing the signal velocity, strength, and shape. We found small variations in signal velocity (between 0.06-0.07 m/ns) but large variations in both amplitude and shape (either order of magnitude variation or doubling/tripling of attribute values). We see that the GPR response from wetter and more clayey diamicts have both lower amplitudes and lower centroid frequencies than the response from their drier and sandier counterparts. Furthermore, we find that the variation in amplitude and shape attributes are better correlated to the diamicts' material properties than the signal velocity is.

Plain Language Summary

Geological deposits originating from the last ice ages are common on the northern hemisphere, and are usually heterogeneous due to the dynamic nature of glacier advance and retreat. Knowledge about their sand and clay distribution is important to solve a wide range of problems regarding construction, groundwater protection, and cleaning of polluted sites. Borehole drilling can provide information on the millimeter- to meter-scale, but only in or close to the borehole. At highly heterogeneous locations, boreholes spaced a few meters apart might not be enough to understand the three-dimensional geological variation. Crosshole ground-penetrating radar (GPR) uses electromagnetic waves to investigate the subsurface between boreholes, but has mainly been used in sandy environments. In this study, we investigate whether crosshole GPR can be used in clay-rich glacial materials. We compare the velocity, strength and shape of the GPR signals, with both borehole information and a field site excavation. We find that GPR signals travelling through wetter and more clayey materials are weaker and more distorted in shape, than those travelling through drier and sandier materials. Furthermore, we see that measurements of signal strength and shape are more sensitive to changes in the subsurface, than measurements of signal velocity are.

1. Introduction

Diamict deposits, such as tills and sediment gravity flows, cover large parts of the northern hemisphere (e.g. Allred, 2000; Ehlers & Gibbard, 2007; Houmark-Nielsen, 2007, 2010; Kjær et al., 2003; McCabe, 1987; Shaw, 1987). These deposits originate or are derived from the ice advances during multiple glaciations in the Pleistocene and are as a result highly heterogeneous both laterally and vertically, on the millimeter- to kilometer-scale (e.g. Batchelor et al., 2019; Kessler et al., 2012; Kjær, 1999; Klint et al., 2013; Shaw, 1987)

Detailed characterization of the structural and textural properties of diamicts is necessary to solve a wide range of hydrogeological, geotechnical, and engineering problems. The clay content is especially important for groundwater flow and contaminant transport, as it has a high impact on the hydraulic conductivity (Fogg & Zhang, 2016). Even minor heterogeneities with high hydraulic conductivity may form preferential flow paths and dominate flow and transport through the otherwise impermeable clayey diamicts (Beven & Germann, 1982; Harrington et al., 2007; Jørgensen, 1998; Kessler et al., 2013; Nilsson et al., 2001; Sidle et al., 1998). Furthermore, the geotechnical properties of the diamict is influenced by the silt and clay content as well as the compaction due to glacial loading (Allred, 2000; Boulton & Paul, 1976).

Currently, state-of-the-art methods to investigate centimeter- to meter-scale variation in diamicts include borehole logging and sampling, as well as geological descriptions of profiles and excavations. Furthermore, thin section studies of mi-

cromorphology provides information on the millimeter-scale variation (van der Meer & Menzies, 2011). While these methods can provide a high degree of detail, they give a limited description of the 3D structure and variability. Furthermore, geological descriptions are time-consuming and constrained to existing outcrops or destructive ditches/excavations with limited depths of investigation.

Crosshole ground-penetrating radar (GPR) is a minimal-invasive method that has been used to solve hydrogeophysical problems for more than two decades (Eppstein & Dougherty, 1998; Hubbard et al., 1997). In crosshole GPR, two antennae are lowered into different boreholes and an electromagnetic (EM) signal is sent between them. Measuring the differences in the recorded signals provides information about the subsurface permittivity, conductivity, and magnetic susceptibility as these relate to the velocity and attenuation of the propagating EM wave (Annan, 2005).

Due to the attenuating properties of clay (Annan, 2005), crosshole GPR has mainly been used in low-loss environments, e.g.: unconsolidated sands and gravelss (Cassiani et al., 2006; Gueting et al., 2017; Irving et al., 2007; Klotzsche et al., 2013; Lassen et al., 2015; Looms et al., 2008), sandstones (Binley et al., 2002), chalk (Keskinen et al., 2017; Nielsen et al., 2010), and igneous rocks of basaltic, andesitic and granitic composition (Dorn et al., 2012; B. Zhou & Fullagar, 2001).

Depending on survey setup, Crosshole GPR measurements can typically provide information down to the decimeter-scale, and between boreholes located up to 6-7 m meters apart. For further information, Annan (2009) and Cassidy (2009) provide a comprehensive introduction to the theory of GPR wave propagation, while A. Klotzsche et al. (2018) and Slob et al. (2010) provides reviews over the latest developments.

Recently, Looms et al. (2018) successfully delineated sand layers within a clayey diamict. Furthermore, they recorded GPR signals propagating through the clayey sections themselves and observed variations in the signals that coincided with a section having large boulders and a higher sand content. However, a thorough investigation was not carried out. Finally, the authors observed that the signal amplitude was better at delineating the sand layers than the more frequently used signal velocity.

Amplitude and velocity are two of many possible radar wave attributes. Attribute analysis is common in reflection GPR (e.g. Bradford, 2007; Benedetto and Benedetto, 2011; Wunderlich and Rabbel, 2013). However, it is less prevalent in crosshole GPR and the number of attributes are often few, e.g.: Z. Zhou et al., (2020) and Klotzsche et al. (2012) uses a combination of velocity, total trace amplitude, and number of wave cycles to detect wave guides in a sand aquifer, while Liu et al. (1998) uses the spectral shift method to determine the attenuation.

This study answers three novel research questions: 1) How does the variation in diamict texture influence the GPR wave response? 2) Which signal attributes

are best at quantifying the differences in the observed radar responses from clayey diamicts? 3) To which degree, can crosshole GPR data provide detailed information on the decimeter- to meter-scale variation within the diamicts?

We do this by comparing our recorded radar responses, in both time and frequency domain, with a comprehensive geological description of the field site, using geological excavation down to 4 m depth as well as sedimentary logging and dense core sampling down to 10 m depth. Finally, we discuss the amount of subsurface information that crosshole GPR can provide in a clay-rich environment such as glacial diamicts, both in itself and together with borehole information.

2. Methods

2.1. Field Site

The Holbæk field site is located outside Holbæk, Denmark (Figure. 1) on a local topographic high in a hummocky moraine landscape (55°42'12.7"N 11°41'01.2"E). The site was formerly agricultural land but is now a meadow with grassy vegetation used for recreational purposes.

We collected the data presented in this study during the summer of 2018. Core sampling, borehole installation, and field site establishment were carried out from 28th May to 3rd July, while the GPR data collection campaign ran from 13th July to 23rd July. The weather was stable during this period. Due to the 2018 European draught, 16.3 mm of precipitation fell between 28th May and 23rd July (Cappelen (ed), 2019; DMI, 2022) leading to a slowly falling water table measured in HOL5 (11 cm from 13th to 23rd July, from 7.75 m.b.g.s. to 7.86 m.b.g.s).

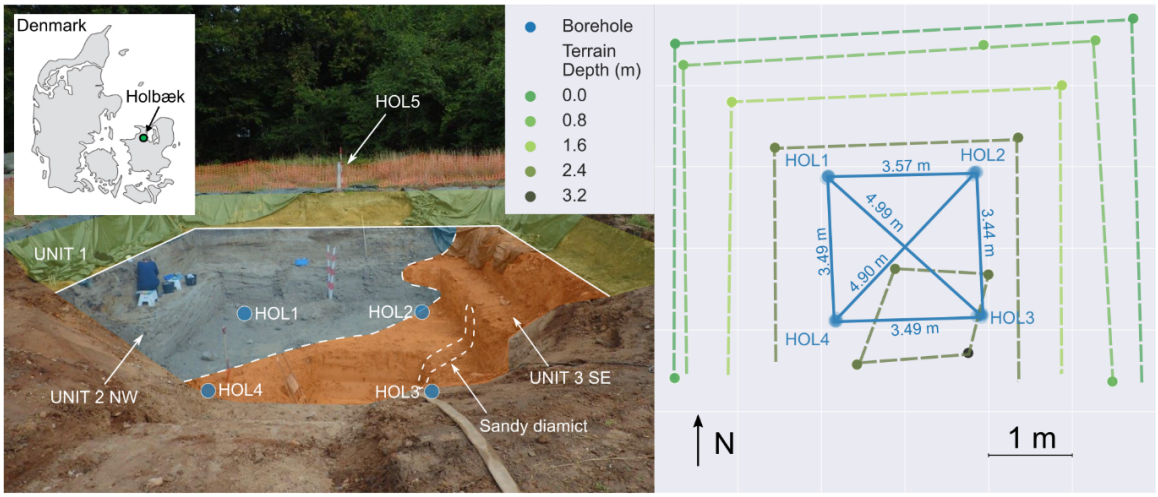

The Geologic Survey of Denmark and Greenland (GEUS) excavated the site later

that summer as part of the CLAYFRAC project (Aamand et al., 2022). This provided a unique opportunity for geological ground truthing down to 3-4 m depth.

Figure 1 – Field site overview. Left: Picture of excavation pointing directly north. The colored overlay corresponds to the geological units in Figure 3, column 5. Right: Position of boreholes and excavation walls. Dots mark GPS measurement points, lines are hand drawn. Blue: Boreholes and GPR profiles. Greens: Excavation corners and walls. The access borehole for groundwater table measurement (HOL5) is only shown in the picture to the left.

A schematic representation of the Holbæk field site is shown in Figure. 1. Four boreholes, HOL1, HOL2, HOL3, and HOL4, were placed in an approximate square geometry within the designated excavation area and a fifth borehole, HOL5, was placed one meter outside the excavated area. Sediment cores were collected from HOL1-4, while HOL5 was auger drilled and sediment samples were collected for every meter. All borehole drilling was done without drilling mud and casing. We expect our sediment cores to give a more accurate representation of the geology, than the disturbed samples from auger drilling. However, both methods are vulnerable to sediment collapse, due to the non-cased boreholes.

HOL1 and HOL2 were drilled to 12.25 m depth and fully cored. HOL3 and HOL4 were drilled to 8.25 m and 11.25 m respectively, with no core recovery between 6.25-8.25 m in HOL3 and 5.25-6.25 m and 7.25-11.25 m in HOL4. Instead, the lacking intervals were sampled with auger drilling. HOL5 was drilled to 12.25 m depth. Due to drilling techniques, no samples or cores were collected between 1.00 m and 1.25 m depth in any of the boreholes, as a connector was needed between the auger drill/core sampler and the drill rods.

Plastic access tubes were installed in HOL1-HOL4 for crosshole GPR measurements. The final installation depth was less than the drilled depth, due to borehole wall collapse, limiting the investigation depth to 10 m. In HOL5, one access tube, filtered from top to bottom, was installed for the measurement of groundwater table depth.

Previous studies by Peterson (2001) and Lassen et al. (2015) demonstrated that it may be important to correct for borehole inclination in crosshole GPR studies. However, the diameter of the boreholes prevented logging of well inclination. While we cannot rule out minor borehole deviation of a few centimeters, our velocity data does not show the same varying trends with depth as Lassen et al. (2015) suggesting that borehole deviation is not a strong source of uncertainty.

2.1. Sediment Samples

We sampled the sediment cores every 10 cm and due to varying core recovery (between 90-100 cm per m of drill depth), the number of samples per core varies. The recovered core material is assumed to represent the bottom of the 1 m core sections, and data gaps may therefore arise at the top of the core sections.

The sampling was done by pressing a small metal cylinder with a known volume (d = 15.13 mm, h = 14.97 mm) into the split core surface. The cylinder was pressed deeply into the core to limit the effect of evaporation from the core surface and excess material was removed while care was taken to minimize compaction of the sample during the process. In sections where the core sample were less cohesive, usually the more sandy sections, we filled the cylinder with extra material from the core. A maximum of 10% of the total sample volume was filled this way, otherwise a new sample was taken.

Volumetric water content ( ) and bulk density (ρ_{bulk}) was measured by weighing the samples before and after freeze-drying for approximately 24 hours. However, it is important to note that we might underestimate the water content of the high-K materials for two reasons: 1) High-K materials will typically have low retention properties and result in water loss during the slicing of the core casing. 2) High-K materials will lose more water due to evaporation during sample preparation in the laboratory than low-K materials.

Grain size distribution was measured less densely than and ρ_{bulk}. Between 2-9 m depth, we selected approximately four samples per core giving a mean sample distance of 25-30 cm. Above and below, we selected two samples per core. (See supplementary material for all sample positions and grain size results).

Each sample was analyzed using the following steps:

1. Wet sieving the clay and silt fraction (<63 µm) from the sand and gravel. The clay and silt fraction was kept in suspension for later use and the fraction was calculated by the weight of the total dry sample minus the weight of the dry sand and gravel fraction.

2. The sand and gravel fraction were then dry sieved using sieves of doubling diameter from 63 µm to 2 mm. Any clay and silt not successfully separated during the wet sieving were added to the calculated weight of the clay and silt fraction.

3. Finally, the clay and silt fractions were measured by laser diffraction using a Malvern Mastersizer on a subset of the samples selected for grain size analysis, i.e. all the samples from HOL2 and three samples between 6-7 m in the other boreholes. Sodium pyrophosphate (0.002M) was added to the clay/silt/water mixture to prevent flocculation and the mixture was suspended using ultrasound. A subsample of 1-2 ml was then acquired with a pipette and measured. The measured clay and silt fractions were then recalculated to correspond to the fraction of the total dry sample.

The weight of the sand and gravel fractions differed slightly from Step 1 to Step 2, giving a measurement error of: µ = 0.18%, = 2.31%, min = -10.64 % max = 6.79 %. In our analysis, we use the total weight of sand and gravel fraction from Step 2. Taking the fraction <63 µm into account, the total measurement error for the sample weight before and after grain size analysis is: µ = - 0.07 %, = 1.24 %, min = -3.55 %, max = 8.72 %.

Using the above-mentioned procedure, we ended up with the following grain size fractions: clay (<2 µm), silt (<63 µm), fine sand (63 µm < 250 µm), medium sand (250 µm < 500 µm), coarse sand (500 µm < 2 mm) and gravel (2mm). However, we only present results from the combined clay and silt fraction, for two reasons: 1) We found a linear correlation between the clay content measured with laser diffraction and the clay and silt fraction measured by a sieve analysis (see supplementary material). The clay and silt curve from the sieve analysis is therefore a good proxy for the overall clay content, with the clay constituting ~22.5 percent of the clay and silt fraction. 2) Subdivision of the sand and gravel fractions did not provide extra information concerning the GPR measurements.

Finally, it should be noted that our sampling strategy poorly samples the fine and medium gravel fractions (4 - 16 mm) and does not sample the coarse clasts such as coarse gravels and cobbles commonly found in diamicts, due to sampler size and dimensions. The motivation was to ensure a known volume for correct water content estimation, and the grain size distributions should therefore be viewed as representative of the matrix and not necessarily the bulk formation.

2.2. GPR Acquisition and Processing

We collected 100 MHz GPR data using the PulseEKKO GPR system from Sensors and Software. We used two survey routines: 1) Calibration measurements in the air at steps of 10 cm separation to determine Absolute Time Zero (ATZ), the exact time the transmitter emits the signal (Oberröhrmann et al., 2013). 2) Zero-Offset-Profiling (ZOP) where borehole antennae are simultaneously lowered 25 cm downhole to maintain no vertical offset. This measurement geometry results in a 1D description of the subsurface. We used a 0.4 ns sampling interval and a 320 ns long time window for each trace.

Subsequently, the following data reduction and processing workflow was used:

1. DC-Correction of individual traces using a semi-automatic picking routine to prepare for manual traveltime picking, but without distorting the signal with filtering. The DC-bias was estimated as the mean of the first 50 indices of each trace (20 ns).
2. Manual traveltime picking of both calibration and ZOP measurements. See the attribute section for picking criteria.
3. Butterworth high-pass filtering (5^{th} order and 10 MHz critical frequency) of raw traces to minimize the low frequency noise and to secondary DC-correct data.
4. Absolute Time Zero (ATZ) correction of band-pass filtered data and traveltime picks.
5. Geometrical spreading correction of amplitudes, assuming a spherical spreading, i.e. multiplication by distance.

Our motivation for picking the traveltimes on the unfiltered but DC-corrected data is to preserve the frequency content and avoid the potential filtering arti-

facts such as signal broadening and precursors. We do observe a good agreement between the unfiltered and filtered data, but re-picking a subset of the filtered data suggests that our picked traveltimes would be faster if the band-pass filtered data had been used for picking.

2.3. Radar Wave Attributes

To quantify the observed wave responses and relate them to the physical parameters of the subsurface, we tested several different radar wave attributes in both the time domain and the frequency domain.

The radar attributes can be divided into three different categories, describing how fast the signal is, how strong the signal is, and which shape the signal has. The first category of traveltime and velocity attributes can only be measured in the time domain, but signal strength and shape can be measured in both the time and frequency domain. Furthermore, the division between the two categories is not sharp as many of the time-domain amplitudes and frequency attributes contain information about both signal strength and shape. In this study, we generally use time domain amplitudes to describe signal strength, and frequency domain attributes to describe signal shape.

The choice of attributes is non-trivial, as several attributes might share the same name while varying slightly in the definition. These differences might seem insignificant when using a theoretical or numerical approach, but they can be crucial when working with field data: Signal-to-noise ratio, sampling and discretization, normalization requirements, and the possibility for automatic picking routines can all favor or hamper a certain attribute and hence affect the feasibility of the overall study.

Figure 2 shows a signal in both the time and frequency domain, together with an illustration of the attributes we selected for this study. We use power spectra for our frequency domain analysis to suppress low amplitude noise. Furthermore, we limit the attribute calculation to the 20-400 MHz band: The lower limit is to remove pronounced noise at ~10-15 MHz (see Figure 5) and the upper limit is to remove any high frequency noise. Lastly, we use trace-normalized power spectra, i.e. spectra where the bin values are normalized to each spectrum's maximum value. This separates the signal strength information from the frequency domain signal shape attributes.

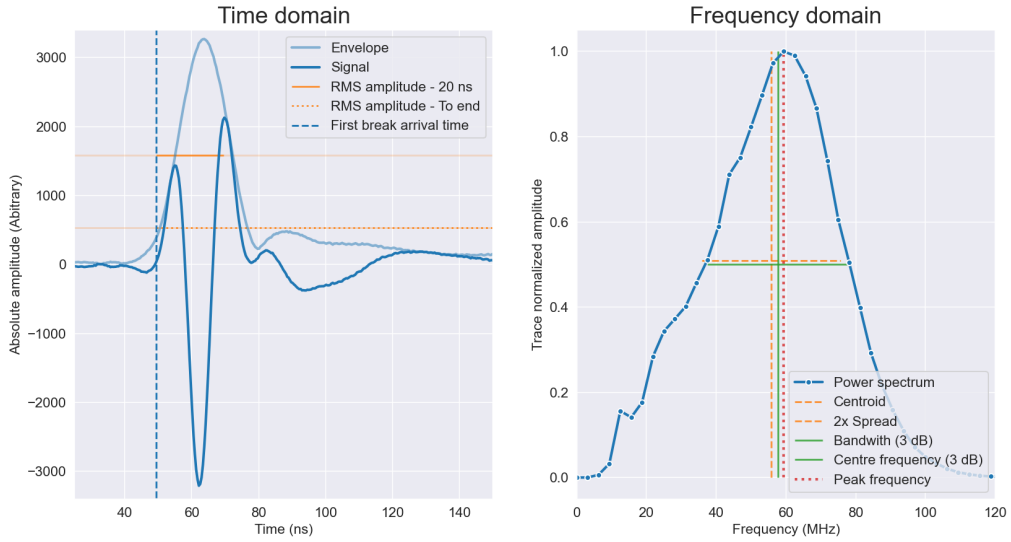

Figure 2 – Illustrations of a wavelet and some of its attributes in both time (left) and frequency domain (right). Time domain: Positive/negative peak amplitudes and maximum envelope amplitude are visible but not annotated. The fully colored parts of the RMS amplitudes show the time windows used for RMS calculation: 20 ns time window after first arrival (Full line) and from first arrival to end of trace (Dotted line). Frequency domain: Skewness, kurtosis, and relative information are not annotated.

2.3.1. Traveltime and Velocity

We use the first break criteria as the arrival time. This attribute is defined as the first time the energy of the signal is detectable. We therefore manually pick the first break arrival and estimate our picking error to +/- one sample, i.e. 0.4 ns.

In theory, the first break traveltime should be the least affected by dispersion effects (Molyneux & Schmitt, 1999), but may with field data be the most challenging to determine exactly for the following reasons: 1) ATZ must be determined. This is traditionally done with separate measurements in air and therefore does not consider any potential borehole coupling effects. 2) Determination of antenna separation distance is critical. 3) White and low frequency noise, as well as precursors hamper the traveltime picking.

Finally, the assumptions regarding the EM wave propagation have a large impact on velocity estimation (Hansen et al., 2014). We only use ZOP data and assume a straight ray propagation for our calculations: The presented velocities are therefore *apparent velocities* and biased towards low velocity values.

2.3.2. First and Second Positive Peak Amplitude

We define the peak amplitudes as the local maxima and minima for the wavelet in question. We separate the peaks into positives and negatives and number them in order of arrival time, i.e. first positive and first negative peak, second positive peak and second negative peak, etc. As a convention, we define normal polarity as the first positive peak arriving before the first negative peak.

2.3.3. Signal Load

Calculation of differences between peak amplitudes can be used as a measure of wavelet shape in the time domain. A frontloaded signal carries most of the energy at the start of the signal, whereas a backloaded signal carries most of the energy at the end of the signal. To estimate this change in wavelet shape in the time domain, we calculate the difference between the second and the first positive peak amplitudes as a percentage of the first peak amplitude.

2.3.4. Maximum Envelope Amplitude

The envelope of the signal represents the instantaneous amplitude of the signal, and it is a measure of the signal energy as a function of time (Yilmaz, 2001, p. 1906-1907). The purpose of using the envelope amplitude is to develop a measure of signal strength that is less dependent on signal shape. It is calculated by taking the absolute value of the Hilbert transformed trace. We use the global trace maximum as the maximum envelope as we have no trailing high-amplitude noise or spurious late arrivals.

2.3.5. Root-Mean-Square (RMS) Amplitude

The-root-mean square (RMS) amplitude is a measure of the "average" wavelet amplitude: It represents the amplitude of an equivalent DC-signal (constant signal). It therefore depends on the total signal length. We have investigated two variants; either calculating the RMS amplitude of the 20 ns window after the first arrival, or the full RMS amplitude from first arrival to the end of the trace. There are advantages and disadvantages to both methods, see discussion for details.

2.3.6. Peak Frequency

The peak frequency is a measure of the central tendency of the signal and is the frequency that carries the most energy, e.g. has the highest amplitude/power.

2.3.7. Bandwidth

The bandwidth of the signal is a measure of the overall frequency content of the signal and hence the wavelength and resolution of the radar wave. The bandwidth is defined as the range of frequencies near the peak frequency that stays above a certain threshold. We use a halving of the amplitude as a threshold, i.e. a -3 dB bandwidth calculated on the power spectrum or a -6 dB bandwidth on the amplitude spectrum.

2.3.8. Center frequency

The center frequency is a measure of the central tendency of the signal, and is the midpoint of the bandwidth. As noted by (Annan, 2019), it is a common mistake not to differentiate between the peak and the center frequency.

2.3.9. Centroid, spread, skewness, and kurtosis

Another way to analyze the frequency spectrum is to use the similarities between frequency spectra and statistical distributions. That way we calculate the statistical moments of the spectrum. Note the differences in naming: 1) The spectral centroid is the arithmetic mean. It is similar to the center frequency. 2) The spectral spread is the standard deviation and is similar to half a bandwidth. We therefore double our reported spreads to make them comparable.

2.3.10. Relative information

Utilizing the similarities between frequency spectra and probability densities, we can measure how similar in shape two frequency spectra are by calculating the relative (Shannon) information. According to (Tarantola, 2005), it is defined as:

$$I\left(S_1 : S_2\right) = \sum S_1 \bullet log\left(\frac{S_1}{S_2}\right) \quad \text{(Eq. 1)}$$

, where S_1 is the first spectrum and S_2 is the second spectrum. Both S_1 and S_2 are normalized to sum to one. The unit of relative information changes depending on the logarithm used. In this paper, we use log2 and therefore calculate the relative information in bits. The larger the relative information is, the larger the difference in shape between the two spectra. We use the 100 MHz data-driven wavelet from air measurements (Svendsen et al., 2020) as a reference spectrum for all calculations, thereby measuring how similar all the recorded waves are to an airwave.

2.3.11. Other similar attributes

The results presented here, are based on the attributes above, except for the RMS amplitude, which is so commonly used in other studies that it warranted an introduction. However, we tested several other attributes that were either similar in definition or frequently used in the literature. The results of these additional attributes were highly correlated to the results arising from the selected attributes. Therefore, they are not included, as they do not provide more information about the subsurface. A comprehensive list of all the tested attributes along with the correlation crossplot can be found in the supplementary material.

2.4.1. Attenuation Estimation

A common way to characterize the interaction between EM waves and materials is by determining the attenuation coefficient ( ) of the specific materials. Assuming far-field conditions, Zhou and Fullagar (2001) state that the measured

amplitude (A_m) is related to the attenuation coefficient ( ) in a homogenous and isotropic medium by:

$$A_m = A_0 e^{-\alpha(r)} \sin(\theta_{\text{tx}}) \sin(\theta_{\text{rx}}) / r \quad \text{(Eq. 2)}$$

where A_0 is the source strength, r is the ray path length, $\sin(\theta_{\text{tx}})$ and $\sin(\theta_{\text{rx}})$ describe the transmitter radiation pattern and receiver sensitivity, and θ is the angle between the ray path and long axis of the given antenna.

For ZOP surveys $\theta_{\text{tx}} = \theta_{\text{rx}} = 90$, which removes the influence of the antennae orientation. After log-linearizing, we get:

$$\ln(A_m r) = -ar + ln(A_0) \quad \text{(Eq. 3)}$$

where $A_m r$ is the measured amplitude corrected for geometric spreading. a has units of 1/m (nepers) with high a values for high attenuating materials. We can estimate a and $\ln(A_0)$, provided we have amplitude measurements at several distances. The ZOP survey used in this study is not ideal for estimating the attenuation, as it effectively only provides two measurement distances, ~3.5 m (sides) and ~5.0 m (diagonals). Nonetheless, we try to estimate the attenuation coefficient, as the clay content of the diamicts is expected to have a large effect on the attenuation properties. We use the envelope maximum amplitude for the attenuation estimation, see later discussion for details. While we estimate the attenuation at the 25 cm depth increments, we estimate the mean a and $\ln(A_0)$ for each of the geologic units presented in the next section. The two lateral adjacent units, Unit 2NW and Unit 2SE, therefore share the same diagonal measurements, but have different side measurements.

3. Results

3.1 Geology

Figure 3 shows the interpretation of the geology within the crosshole GPR investigated volume at the Holbæk field site. This interpretation is based on the knowledge of the regional setting, geological excavation, borehole descriptions, and sediment samples. Overall, the site is highly heterogeneous both laterally and vertically, as expected for hummocky moraine landscapes (Selsing, 1980; see also Kjær and Krüger, 2001), but can be divided into five units as described in Table 1.

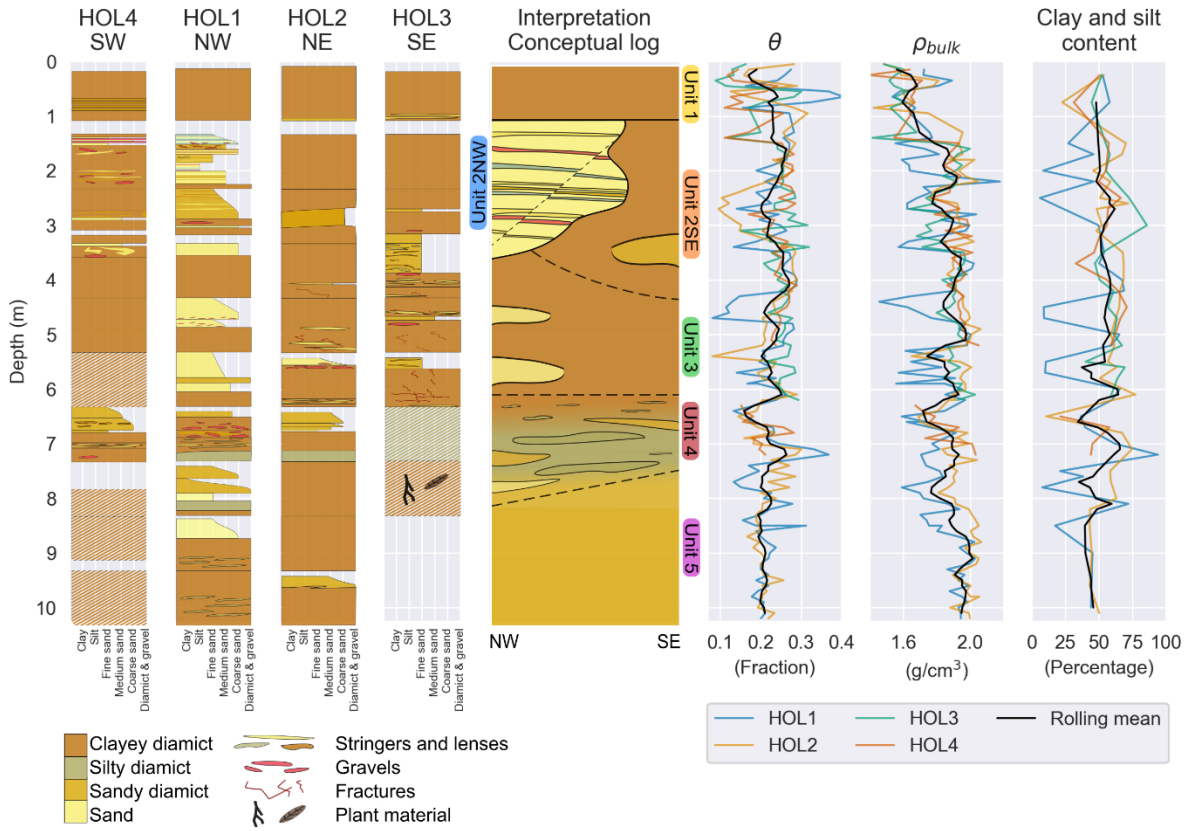

Figure 3 – Integrated geologic interpretation (Column 5) of the available data: Sedimentary logs (Columns 1-4), sediment samples (Columns 6-8), and the geologic excavation (Figure 1, left). Below the 10 m GPR investigation depth, Unit 5 is interpreted to continue to at least 11-12 m in HOL1, HOL2, and HOL4. Note that the color of Unit 5 is not present in the sedimentary log legend, as it is used to indicate that Unit 5 is sandier than Unit 2 and 3, but still classified as a clayey diamict.

Sedimentary logs: Fully colored log marks cored interval, hatched log marks auger sampled interval. Sandy diamicts follow the grain size scale to indicate dominant grain size, whereas silty and clayey diamicts are marked as diamicts to distinguish from pure silts and clays. Intervals are to scale, whereas details such as gravels, stringers, and fractures are enlarged but constrained vertically to stay within depth interval.

Sediment samples: Color corresponds to the different survey boreholes, and not the color scheme used to mark the geological units in Column 5. To take the uneven sample spacing into account, the rolling mean (black line) is calculated from linearly interpolated values. Full grain size distributions can be found in

the supplementary material.

Table 1

Sedimentary Description of Geologic Units

Unit name	Interval (m.b.g.s.)	Description
	Top: 0 Bottom: 1 m	Soil (5-20 cm thick) gradually changing into a clayey diamict with locally high sand content. Horizontal layering can occur towards the bottom of the unit. Sharp horizontal boundary to Unit 2NW and 2SE.

Unit name	Interval (m.b.g.s.)	Description
2NW	Top: 1 m Bottom: 3.5 m	Layers of sorted and well-sorted clays, silts, and sands, and unsorted diamicts of varying thickness. Internally faulted. Wedged shaped toward HOL2 and HOL4 and overlies Unit 2SE. Interpreted as ice-lake deposits. (Aamand et al., 2022) Though not resolvable in grain size curve, the layering and sorting is clearly present in the cores. Located in the north-western corner of the excavation and seen in HOL1, HOL2, and HOL4 (Debris flow only). The unit has a sharp boundary to Unit 3 and a sediment gravity flow marks the boundary towards 2SE in the excavation. The gravity flow is not present in HOL1, but is visible in HOL4 and possibly HOL2.

Unit name	Interval (m.b.g.s.)	Description
2SE	Top: 1 m Bottom: 4 m	Clayey diamict with moderate sand content (approximately 40-50 percent). A lens of sandy diamict (less than 50 cm wide) dips towards the south in the eastern part of the excavation, between HOL2 and HOL3, and is present in HOL3 at 3.5 m depth. Located in the south-eastern corner of the excavation and seen in HOL2, HOL3 and HOL4. Underlies Unit 2NW The unit has a gradational boundary to Unit 3.

Unit name	Interval (m.b.g.s.)	Description
	Top: 3.5-4 m Bottom: 6-7 m	Clayey diamict. Matrix has low to moderate sand content (30-40 percent) and a moderate clay content (18 percent). Stringers, lenses and layers of sandy diamict and sand are present in the interval, most predominant in HOL1, where two 40-50 cm thick intervals are present. These layers have internal grading, are well-sorted to sorted, and can dip in relation to the core samples. We therefore interpret these as in-situ samples and not a result of borehole collapse or downfall. Unit 3 has a gradational boundary to Unit 4.

Unit name	Interval (m.b.g.s.)	Description
	Top: 6-7 m Bottom: 7-8 m	Transitional unit. Very silty clayey diamict to actual silty diamict. The silty diamict occurs both as 10-20 cm thick units and as dispersed striations in the very silty clayey diamict in HOL1 and HOL2. Layers of sandy diamict occurs at varying depth in this interval as well. The auger drill samples between 6.25 – 7.25 m only shows silty diamict and show signs ductile deformation. However, it is hard to determine whether this is a pristine sample or if the ductile deformation is a result of auger drilling. Being a transitional unit, the boundary to Unit 5 is gradational.

Unit name	Interval (m.b.g.s.)	Description
	Top: 7-8 m Bottom: 12 m	Clayey diamict with moderate to high sand content (50-55 percent), moderate to high silt content and low clay content (10-12 percent). A large amount of plant material is observed in the auger drill samples from HOL3, suggesting the presence of a sediment gravity flow. Grain size was not measured below 10.25 m but cores from HOL1 and HOL2 and auger drilling from HOL3 suggest the unit continues to at least 12 m. Internal layering in the clayey diamict is observed in HOL1 at 10.25 m depth.

It is important to notice that we do not observe large variations in bulk density and only see some variation in water content. Except for the increase in bulk density between 1–2 m depths, the bulk density increases only gradually with depth, from ~1.8 g/cm^3 to ~2 g/cm^3, suggesting a lower porosity with depth most likely due to compaction. Likewise, we see an average volumetric water content of approximately 0.25 in the upper parts of the studied section that decreases to 0.20 below 6 m depth, as a response to the increased bulk density.

Assuming a grain density of 2.65 g/cm^3, we calculate porosity and water saturation (results are not shown here). We find near-saturated conditions in the diamict intervals, even above the measured groundwater table.

While the diamicts are saturated or almost saturated, the sand intervals and some of the sandy diamicts show a larger variation in water content (around 0.10-0.15). Likewise, the sandy intervals, in particular the sorted sands, have lower bulk densities (between 1.50-1.75 g/cm^3) and hence larger porosities. The combined effect of these two properties results in low water saturations in the sandy intervals.

3.2. Ground-Penetrating Radar

In the recorded 100 MHz GPR data, we identify four main radar responses marked by letters in Figures 4 and 5:

1. A high velocity and high amplitude signal with a minor change in the frequency distribution. Observed for the radar waves in the northwestern corner between 2-3 m depth. Possibly beginning already at 1.5 meters depth.

2. A low velocity and low amplitude signal with a large change in the frequency distribution. Observed for radar waves propagating approximately between 4-6 m depth across the whole survey site.

3. An intermediate to high velocity and intermediate amplitude signal with a minor change in the frequency distribution. Observed for radar waves propagating below 5.5-6.0 m depth across the whole survey site. Internally very variable response in both time and frequency domain.

4. An intermediate velocity and low amplitude signal with a minor change in the frequency distribution. Observed for radar waves propagating in the southeastern corner between 2-4 m depth. The signal is strongest and least frequency distorted at approximately 3 m depth.

To quantify the observations above, Figure 6 shows the observed radar wave attributes versus depth.

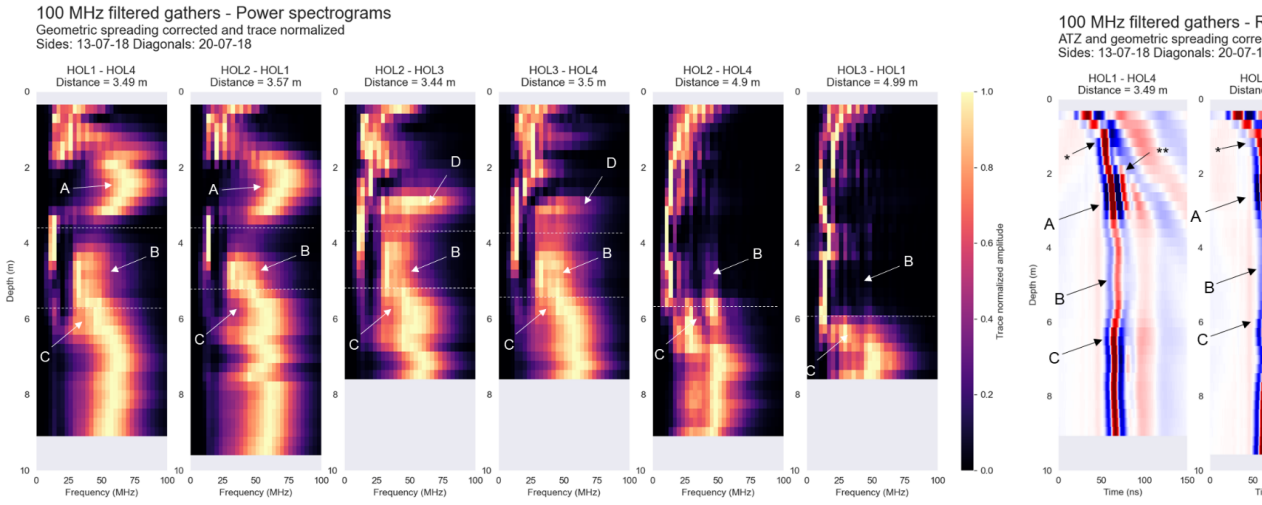

4 – 100 MHz Crosshole GPR Zero-Offset-Profiles (ZOPs) through a hummocky moraine succession. The ABCD captions correspond to bullets in the text describing the different radar responses. The first four columns are the sides of the survey setup and are organized as west, north, east, and south. The last two are the diagonals.

Top: Radargrams showing variation in radar response with depth in the time

domain. Amplitude is absolute but in arbitrary units. Single asterisk marks the first detection of direct arrival while still heavily interfering with the refracted airwave. Double asterisk marks the first trace where direct arrival is clearly separable from refracted airwave.

Bottom: Power spectrograms showing the variation in radar response with depth in the frequency domain. Spectrum amplitudes are trace-normalized, i.e. against maximum trace amplitude. Dotted lines mark the broad transition from one radar response to another.

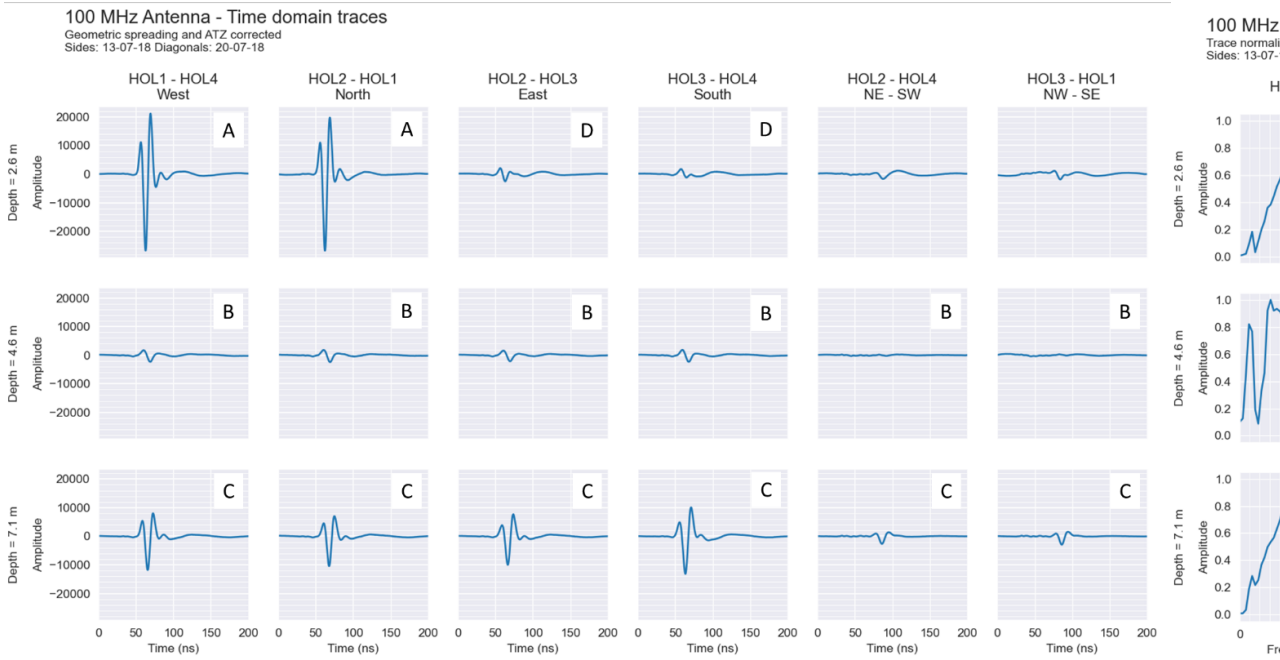

5 – The same crosshole GPR data as Figure 4 but now only showing three traces (top) and spectra (bottom) for each profile (columns) at three selected depths: 2.6, 4.6, and 7.1 m (rows). The ABCD of each panel corresponds to the bullets in the text and captions in Figure 4. Panels without letters are ambiguous to interpret due to low signal-to-noise ratio. Note that the two diagonal measurements at 4.6 m depth contain a signal similar to Response B, but the amplitude is not large enough to be seen on the chosen axis y-axis limits.

By comparing the results from Figures 3-6, we see that the four different radar responses match the observed geological units. Response A corresponds both laterally and vertically to the extent of Unit 2NW (ice-lake deposits). Response B approximately corresponds to Unit 3 (clayey diamict), while Response C corresponds to both Unit 4 (transitional unit) and Unit 5 (sandier clayey diamict), and finally, Response D corresponds to Unit 2SE (Clayey diamict). We cannot

distinguish Unit 1, as the radar responses at this depth are interfered by refracted arrivals. This interference also influences Response D: This is especially clear in Figure 5, where response D shows a pronounced low frequency peak, between 10-20 MHz.

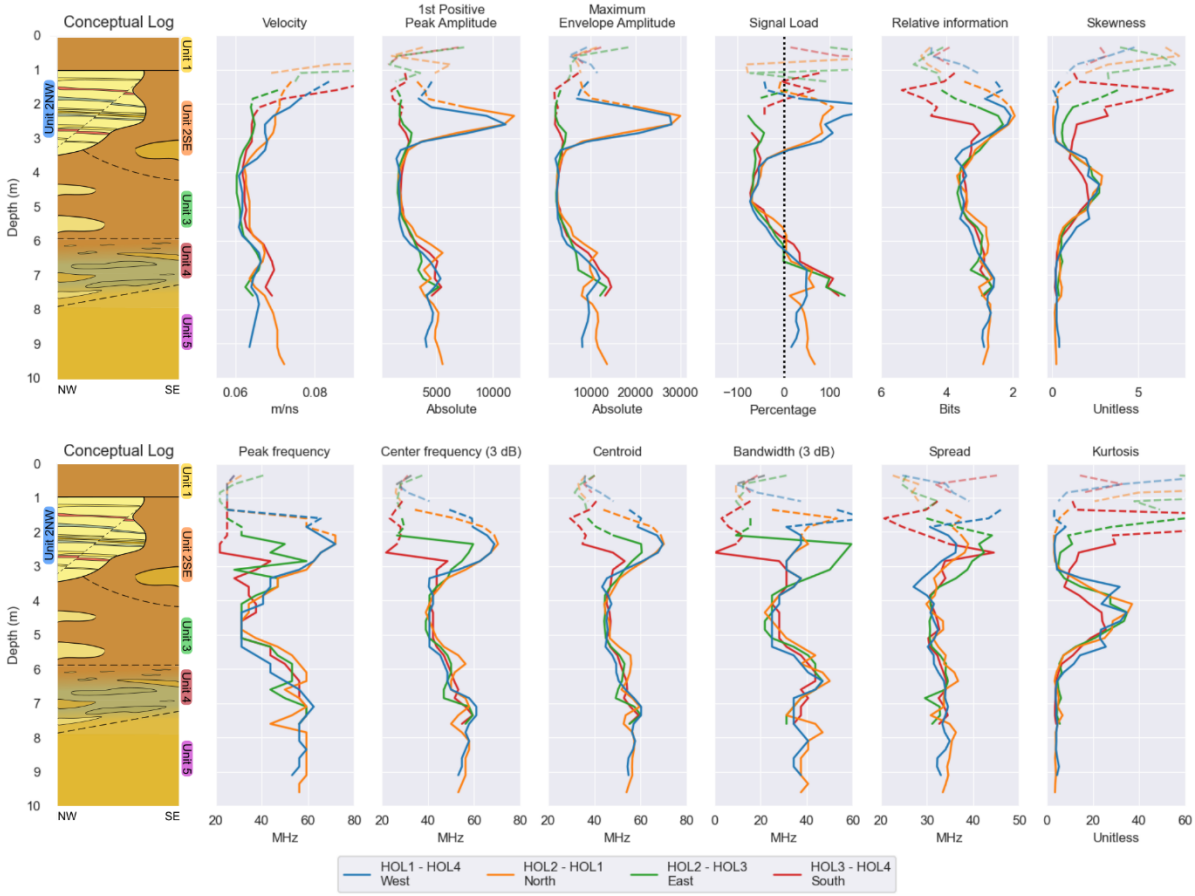

Figure 6 – Calculated attributes versus depth for the GPR profiles shown in columns 1-4 in Figure 4. The attributes for the diagonals are omitted here due to low signal-to-noise ratio, but can be seen in the supplementary materials. The first positive peak amplitude and maximum peak amplitude are given in absolute but arbitrary units.

The black dotted line in the signal load log marks the boundary between front-loaded (left) and backloaded (right) signals. The spread is multiplied by two, for it to be similar to the bandwidth. The relative information is plotted with an inverse x-axis to emphasize that less distorted signals, have a higher similarity with airwaves (low relative information) than signals that are highly distorted/attenuated.

The possible interference with the critically refracted airwave is marked in three ways: Fully colored lines mark measurements where the direct arrival is fully distinguishable from any critical refracted arrival (after the double asterisk in Figure 4). Fully colored but dashed lines mark measurements where the direct arrival is the first arrival but may still be interfered by the critical refracted airwave (between the single and double asterisk in Figure 4). The transparent and dashed lines mark measurements where it is impossible to distinguish between the direct and refracted arrival (above the single asterisk in Figure 4).

In the time domain, we see the largest variation in radar response when looking at the amplitudes. Depending on the chosen amplitude attribute, the amplitudes vary by one or two orders of magnitude within the diamict units, whereas when comparing the response from Unit 5 with the response from Unit 2NW, we see a doubling or tripling of amplitudes. The effect is largest for the second positive peak amplitude and smallest for the envelope amplitude, emphasizing that the signal changes shape from unit to unit.

The velocities vary much less, with low values around 0.060-0.063 m/ns between 4-6 m depth (Unit 3) and high values around 0.070-0.071 m/ns between 2-3 m depth in the north-western corner (Unit 2NW) and below approximately 6.5 m depth (Unit 4 and Unit 5). From the velocities alone, it is difficult to distinguish Unit 2NW from Units 4 and 5.

Looking at the signal load in the time domain, Figure 4 and 5 top, we notice that the signals recorded through Unit 2SE and Unit 3 (Response B and D) are all front-loaded, whereas the rest of the recorded signals (Response A and C) are all middle- to back-loaded. In Figure 6, row 1, column 4, we see that the first zero crossing occurs sharply at 3.5 m, i.e. the contact interpreted between the sandy ice-lake deposits of Unit 2NW and Unit 3. The second zero crossing is broader occurring between 6-7 m corresponding to the top of the transitional Unit 4.

In the frequency domain, we generally observe large downshifts in frequency with center and peak frequencies lying in the 20-70 MHz range compared to the 100-120 MHz airwave.

Overall, the measures of central tendencies (peak frequency, centroid, and center frequency), the bandwidth, and the relative information show similar trends as the time domain attributes, as the changes with depth correspond to the interpreted geological boundaries. The kurtosis and skewness differ from the other frequency attributes by being most sensitive to the extremely non-Gaussian spectra occurring between 3-6 m depth (Unit 3).

Finally, measuring the spread does not provide meaningful information about the subsurface despite its similarity to the bandwidth attribute. This could be due to the non-Gaussian frequency distributions, best seen in Figure 5.

The frequency spectrum is calculated on the entire signal. As a result, the frequency attributes are more affected by different waveform arrivals, such as

reflections, refractions, and wave guiding effects, than many of the time domain attributes. This is especially seen in Figures 4 and 6 down to approximately 2 m depth, where the refracted airwave interferes with the direct arrival.

Furthermore, the peak frequency, bandwidth, and center frequency all appear more jagged than the other frequency domain attributes. This is due to the rather coarse discretization of the frequency spectrum (3.125 MHz), as these attributes either are limited to or affected by the bin discretization.

The main differences, between the time domain and the frequency domain attributes, are found between 2.5-3.0 m depth in the south and east profiles (red and green lines in Figure 6). At these depths, the frequency attributes have higher values that correspond with sandier material, while the amplitude attributes have very low values that correspond to more clayey material. This confirms that crosshole GPR can separate Units 2NW, 2SE, and 3 from each other.

3.3. Estimation of Material Porperties using Radar Wave Attributes and Attenuation

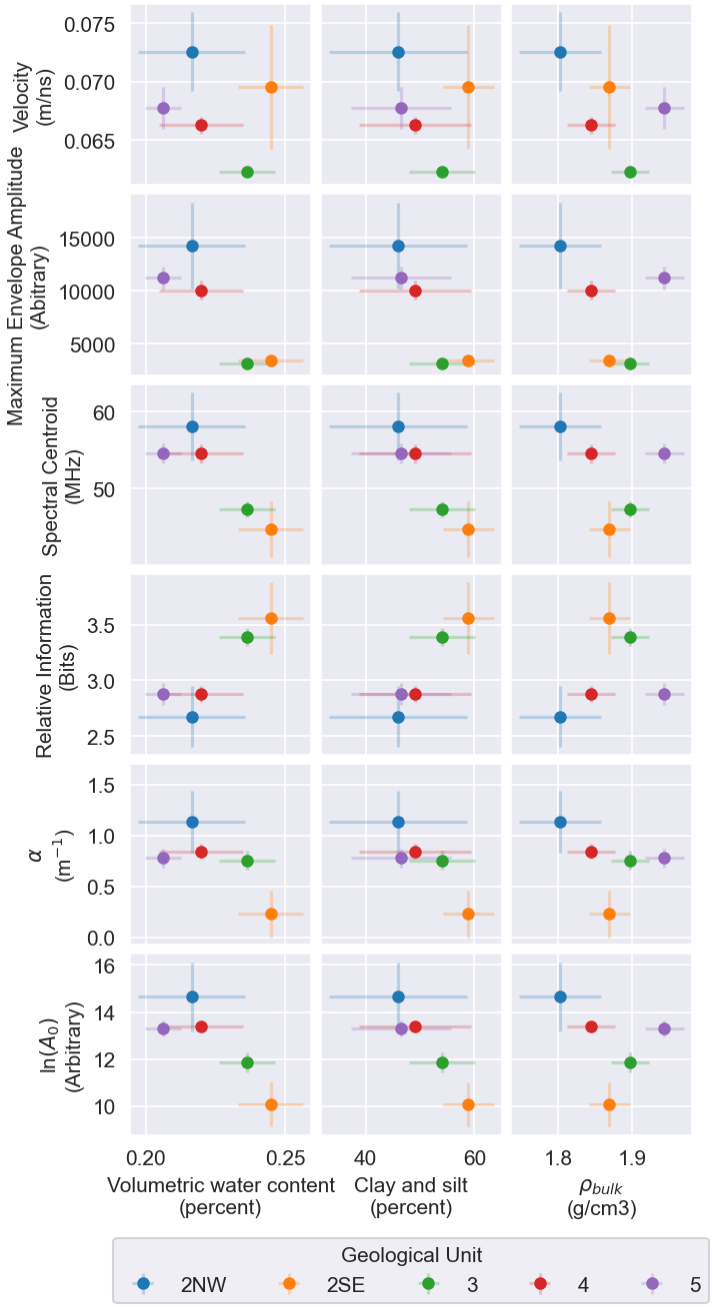

The sensitivity range (referred to as kernel) of crosshole GPR method in clay-rich diamicts is unknown, but we expect it to be substantially larger than the centimeter-scale sampling of the geological properties.

Figure 7 – Selected radar wave attributes versus sediment properties, grouped by geological units. Scatters show the means and bars show the standard error with 95 % confidence interval. Geological Unit 1 is not shown, as the radar data is too influenced by the critical refracted airwave. Note that the attenuation data for Unit 2NW and Unit 2SE share measurements due to survey setup and are therefore correlated. See method section for details.

To overcome this challenge, we have grouped our data by geological unit, as seen in Figure 7. It shows the mean attributes measured within each unit plotted against the mean of the different material properties.

As the sensitivity kernels overlap, the GPR attributes are not independent samples, which could lead to an underestimation of the confidence intervals. On the other hand, the GPR measurements on the boundaries of the geological units sample both sides of the boundary, which could lead to an overestimation of the confidence intervals.

In general, we can see that the attribute means correlate with the mean water content and mean clay and silt content of the units, whereas we observe no clear relation between the mean bulk densities and the mean attributes.

Grouping the data this way, we see that geologically similar units plot close to each other in attribute space. The diamicts with high sand content (Unit 4 and 5) plots close to the sandy ice-lake deposits (Unit 2NW), the two clayey diamicts with each other (Unit 2SE and Unit 3), and lastly there is a tendency that the transition Unit 4 plots between Unit 3 and Unit 5.

The only exception to the above is that the velocity seems to be better correlated with the bulk density than the water content and the clay and silt content. We see that the correlation has the opposite sign of what we expect: Increasing the bulk density decreases the velocity. Increasing the bulk density usually lowers the porosity, which increases the velocity in saturated conditions, but decreases the velocity in unsaturated conditions. While we calculate saturated conditions for the diamicts, we know our measurements are above the groundwater table (minimum 7.76 m depth) and hence air in the pore space might complicate the picture.

Finally, we see that the estimated linear attenuation coefficient ( ) is negatively correlated with the mean water content as well as the clay and silt content. Furthermore, is positively correlated with the signal amplitude. Both of these observations are counter intuitive, as they imply that the strongest signals are observed through the most attenuating materials, which are the driest and sandiest. We also observe that the estimated A_0 is positively correlated with . The source amplitude should in principle be constant unless borehole-coupling effects strongly influence the signal strength, and the underlying assumptions regarding linear attenuation and far-field conditions are therefore questionable at the investigated site.

4. Discussion

4.1. Interpretation of Geology from Radar Response

Overall, crosshole GPR data can provide valuable information about clayey diamicts. The method can distinguish between the different investigated geological units, as the structure and sedimentary texture of each unit produce a uniquely different GPR wave response. Laterally, the delineation is primarily restricted by the given survey setup. However, the approximate extent of the ice-lake deposits is clearly separated from Unit 2SE. The clear delineation of the sand is consistent with the findings of Looms et al. (2018).

Vertically, the method can resolve the different units, which are 2-3 m thick at the investigated site. While the vertical extent of Unit 4 is more difficult to determine exactly from the GPR data, the more gradual change in attribute values from Response B to C indicates the presence of this transition unit. It might have been easier to estimate the vertical extent of Unit 4 had all ZOP profiles extended to 10 m depth.

To improve the interpretation of the geological structure, more knowledge is needed regarding how geological boundaries between diamicts affect the radar response and thereby the resulting radar- and spectrograms, e.g., information on the sensitivity kernel size. Detailed 3D full-waveform modelling could provide this information, and the open-source modelling software gprMax has been successful for reflection GPR previously (e.g. Warren et al., 2016; Koyan and Tronicke, 2020).

However, crosshole GPR in clayey diamicts faces two challenges: First, it is difficult if not impossible to derive information about the top 0-1.5 m depth, due to the effects of the soil/air interface. This prevents the identification of Unit 1, and makes interpretation of Unit 2SE more difficult due to the decreased signal-to-noise ratio. Future research should investigate, whether this could be mitigated by either shielding the boreholes or adding an "absorbing- boundary-condition", e.g. a water basin, on the surface. Especially, as soil/air interfaces effects also influence surveys in low-loss environments (Annan, 2005).

Secondly, the GPR data in our study does not resolve the small-scale heterogeneity, seen here as the up to 50 cm thick sand lenses in HOL1. Likewise, it is difficult to determine the correct boundary depths and dips on the decimeter-scale. However, this is mainly a result of our analysis only including ZOP measurements. It is inherently difficult to derive information about 2D geometry, when using a 1D-averaged geophysical method. The next steps are therefore to use data from multiple-offset-gathers (MOGs) to try to resolve the finer scale structures. However, this implementation is not straightforward. The common and low cost ray-based methods are usually velocity tomograms, which might not provide much information in clay-rich environments. Furthermore, while the more computational expensive full-waveform inversion (FWI) methods have successfully resolved decimeter-scale structures, the attenuation tomograms are still

quantitatively unstable, as they are constrained by the initial model conditions (Klotzsche et al., 2019).

In principle, we were not able to distinguish the geological units based on the sedimentary logs alone, as the small-scale variability down to 4 m depth cluttered the large structural interpretation. To arrive at our conceptual model we needed the information from the excavation to correlate the logs.

Alternatively, our study shows that GPR data can be used for the same purpose. Based on the GPR data alone we would be able to infer the overall geological structure and rank the units according to their relative sand content, providing a context for interpretation of the logs.

4.2. Attribute Analysis for Crosshole GPR Surveys in Clay-Rich Media

We have shown that crosshole GPR surveys benefit from using multiple radar wave attributes rather than relying on a single attribute to provide information about the subsurface. This is especially important as our analysis shows that no single attribute outperforms the others. The attributes all quantify and emphasize different parts of the recorded signal, and hence provide different information about the subsurface.

The frequency attributes are especially suitable for quantifying the changes in signal shape, which seem better at estimating the sediment properties than the time domain attributes and permit the identification of Unit 2SE. However, the frequency attributes seem to have larger sensitivity kernels than the time domain attributes. The fact that these values are calculated from the entire measured trace, could explain the increased kernel size. As a result, they are less suited for the determination of the decimeter-scale structure and more vulnerable to spurious waveforms and transient noise than the time domain attributes. In this study, especially the refracted airwave arrivals down to 1.5 m complicate the interpretation of the frequency domain attributes.

Our analysis shows that some redundancy exists between the different attributes. Below we therefore propose a shortlist of four attributes that provide the most information about high-loss environments:

1. Maximum envelope amplitude as a measure of total signal strength. It is well correlated with the RMS amplitude, is somewhat insensitive to changes in signal shape, and can be automatically picked. Most importantly, the value is independent of time window length and is therefore easier to pick than RMS amplitude in cases with spurious arrivals or poor signal-to-noise ratio.

   Ideally, the signal strength attribute should be a time integral to account for any pulse widening. The RMS amplitude provides such a measure by being a DC-equivalent signal. However, all the time integrals depend on the chosen time window length, which requires expert knowledge when selecting, and usually traveltime picking as well.

2. Signal load as the first measure of signal shape. Signal load is simple to estimate and only requires identification of the first and second positive peak, which is an easily automated task. Furthermore, it is a robust attribute well suited for comparison across and between sites as it is a relative measure of signal shape. Factors that influence the absolute value of the amplitude, such as borehole coupling and transmitter battery power, should therefore affect the signal load less. However, different equipment might emit different source wavelets. Lastly, the categorical nature of signal loading (front/back/equal-loaded) provides objective groupings of radar responses.

3. Spectral centroid as is the second measure of signal shape. Most importantly, it is the best attribute for estimating the mean clay and silt content of the geological units. Furthermore, we believe that the centroid is a good compromise in quantifying the frequency domain. While the range of the centroid values is only slightly smaller than that of the peak and center frequencies as well as the bandwidth, the binning of the frequency spectrum does not influence the spectral centroid.

   The relative information could be a worthy substitute for the spectral centroid. It provides a method of comparing signals with air signals, hence improving the comparison between sites and different equipment. However, the relative information is not commonly used and it integrates all the differences in signal shape to a degree that it risks evening out the differences.

4. Lastly, we believe that the signal velocity is an important attribute for crosshole studies, despite not providing a lot of information at this clay-rich field site. The velocity is well suited for comparison between sites, as it only requires precise determination of the travel distance and ATZ. Furthermore, Looms et al. (2018) showed that signal velocity can provide information at clay-rich sites where the retention properties are different enough to provide variation in subsurface water content.

We did not include kurtosis and skewness in the short list, despite their strong differences from the other frequency attributes. Currently, we do not know whether these two attributes detect some shape feature that is characteristic of highly attenuated signals or just a lack of signal, which is easier to describe using amplitude attributes. Thus, further research is needed to determine their usefulness.

5. Conclusions

We found that clayey diamicts give rise to crosshole GPR responses with low amplitude and distorted signal shape, while more sandy diamicts affect the GPR response to a lesser degree. This study cannot determine unequivocally whether this is a result of the clay itself or the indirect effect of the clay causing higher retention properties and therefore higher water content. However, it is unlikely that the observed small changes in water content, giving rise to only small

changes in EM velocity, would lead to a doubling or tripling in signal strength and frequency content. Nonetheless, at our specific field site, crosshole GPR was able to distinguish between the geological units as the material properties of each unit produced unique radar responses.

Acknowledgments

We thank Geocenter Denmark for funding this study. We acknowledge the CLAYFRAC project at the Geological Survey of Denmark and Greenland (GEUS) for selecting and excavating the survey site. In particular, we thank Peter R. Jakobsen for discussing the excavated geology. Likewise, we would like to thank Bolette Badsberg Jensen for helping with the GPR acquisition. Lastly, the authors declare that we have no conflicts of interest with respect to this paper.

Open Research

A data repository for this study is available at [repository, source name] via [DOI, persistent identifier link] with [license, access conditions]. It contains: 1. The geological data regarding the field site used, i.e. sediment sample descriptions and measurements, pictures of cores and the excavation photograph in Figure 1, as well as the water table measurements. 2. GPS measurements of the survey geometry. 3. The recorded crosshole ground-penetrating data, as both raw data files in proprietary data formats and in various open-source formats. 4. The calculated radar wave attributes. The processing, analysis, and vizualisation was conducted in python and the used python scripts are all found in the data repository. The figures where created using numpy (Harris et al., 2020), scipy (Virtanen et al., 2020), pandas (McKinney, 2010; The pandas development team, 2020), matplotlib (Hunter, 2007) and seaborn (Waskom, 2021). A complete list of dependencies and version control can also be found in the data repository.

References

Aamand, J., Badawi, N., Roll Jakobsen, P., Jørgensen, P. R., Mosthaf, K., Troldborg, L., & Rolle, M. (2022). *Mapping groundwater vulnerability to pesticide contamination through fractured clays - CLAYFRAC*. https://doi.org/978-87-7038-375-2Allred, B. J. (2000). Survey of fractured glacial till geotechnical characteristics: Hydraulic conductivity consolidation and shear strength. *Ohio Journal of Science*, *100*(3–4), 63–72.Annan, A. P. (2005). GPR Methods for Hydrogeological Studies. In Y. Rubin & S. S. Hubbard (Eds.), *Hydrogeophysics* (50th ed., pp. 185–213). Springer.Annan, A. P. (2009). Electromagnetic Principles of Ground Penetrating Radar. In H. M. Jol (Ed.), *Ground Penetrating Radar: Theory and Applications* (1st ed., pp. 3–37). Elsevier.Annan, A. P. (2019). GPR Jargon - How do we say

what we mean? and Glossary of GPR Terms. Retrieved January 5, 2022, from https://sensoft.ca/gpr/gpr-jargon-how-do-we-say-what-we-mean/ and https://www.sensoft.ca/glossary-of-gpr-terms/Batchelor, C. L., Margold, M., Krapp, M., Murton, D. K., Dalton, A. S., Gibbard, P. L., et al. (2019). The configuration of Northern Hemisphere ice sheets through the Quaternary. *Nature Communications*, *10*(1), 1–10. https://doi.org/10.1038/s41467-019-11601-2Benedetto, A., & Benedetto, F. (2011). Remote sensing of soil moisture content by GPR signal processing in the frequency domain. *IEEE Sensors Journal*, *11*(10), 2432. https://doi.org/10.1109/JSEN.2011.2119478Beven, K., & Germann, P. (1982). Macropores and Water Flow in Soils. *Water Resources Research*, *18*(5), 1311–1325. https://doi.org/10.1002/wrcr.20156Binley, A., Winship, P., West, L. J., Pokar, M., & Middleton, R. (2002). Seasonal variation of moisture content in unsaturated sandstone inferred from borehole radar and resistivity profiles. *Journal of Hydrology*, *267*(3–4), 160–172. https://doi.org/10.1016/S0022-1694(02)00147-6Boulton, G. S., & Paul, M. A. (1976). The influence of genetic processes on some geotechnical properties of glacial tills. *Quarterly Journal of Engineering Geology*, *9*(3), 159–194. https://doi.org/10.1144/GSL.QJEG.1976.009.03.03Bradford, J. H. (2007). Frequency-dependent attenuation analysis of ground-penetrating radar data. *Geophysics*, *72*(3).Cappelen (ed), J. (2019). DMI rapport 19-01 Danmarks klima 2018 - with English Summary. *Danmarks Meteorologiske Institut*, *19*(01), 1–95. Retrieved from https://www.dmi.dk/publikationer/Cassiani, G., Bruno, V., Villa, A., Fusi, N., & Binley, A. M. (2006). A saline trace test monitored via time-lapse surface electrical resistivity tomography. *Journal of Applied Geophysics*, *59*(3), 244–259. https://doi.org/10.1016/j.jappgeo.2005.10.007Cassidy, N. J. (2009). Electrical and Magnetic Properties of Rocks, Solids and Fluids. In H. M. Jol (Ed.), *Ground Penetrating Radar: Theory and Applications* (1st ed., pp. 41–67). Elsevier.DMI. (2022). DMI Climatedata [Dataset]. Retrieved January 27, 2022, from https://confluence.govcloud.dk/display/FDAPI/Climate+dataDorn, C., Linde, N., Doetsch, J., Le Borgne, T., & Bour, O. (2012). Fracture imaging within a granitic rock aquifer using multiple-offset single-hole and cross-hole GPR reflection data. *Journal of Applied Geophysics*, *78*, 123–132. https://doi.org/10.1016/j.jappgeo.2011.01.010Ehlers, J., & Gibbard, P. L. (2007). The extent and chronology of Cenozoic Global Glaciation. *Quaternary International*, *164–165*, 6–20. https://doi.org/10.1016/j.quaint.2006.10.008Eppstein, M. J., & Dougherty, D. E. (1998). Efficient three-dimensional data inversion: Soil characterization and moisture monitoring from cross-well ground-penetrating radar at a Vermont test site. *Water Resources Research*, *34*(8), 1889–1900.Fogg, G. E., & Zhang, Y. (2016). Debates—Stochastic subsurface hydrology from theory to practice: A geologic perspective. *Water Resources Research*, *52*(12), 9235–9245. https://doi.org/10.1002/2016WR019699Gueting, N., Vienken, T., Klotzsche, A., van der Kruk, J., Vanderborght, J., Caers, J., et al. (2017). High resolution aquifer characterization using crosshole GPR full-waveform tomography: Comparison with direct-push and tracer test data. *Water Resources Research*, *53*(1), 49–72. https://doi.org/10.1002/2016WR019498Hansen, T. M., Cordua, K. S., Ja-

cobsen, B. H., & Mosegaard, K. (2014). Accounting for imperfect forward modeling in geophysical inverse problems — Exemplified for crosshole tomography. *Geophysics*, *79*(3), H1–H21. https://doi.org/10.1190/geo2013-0215.1Harrington, G. A., Hendry, M. J., & Robinson, N. I. (2007). Impact of permeable conduits on solute transport in aquitards: Mathematical models and their application. *Water Resources Research*, *43*(5). https://doi.org/10.1029/2005WR004144Harris, C. R., Millman, K. J., van der Walt, S. J., Gommers, R., Virtanen, P., Cournapeau, D., et al. (2020). Array programming with NumPy [Software]. *Nature*, *585*(7825), 357–362. https://doi.org/10.1038/s41586-020-2649-2Houmark-Nielsen, M. (2007). Extent and age of Middle and Late Pleistocene glaciations and periglacial episodes in southern Jylland, Denmark. *Geological Survey of Denmark and Greenland Bulletin*, *55*, 9–35.Houmark-Nielsen, M. (2010). Extent, age and dynamics of Marine Isotope Stage 3 glaciations in the southwestern Baltic Basin. *Boreas*, *39*(2), 343–359. https://doi.org/10.1111/j.1502-3885.2009.00136.xHubbard, S. S., Peterson, J. E., Majer, E. L., Zawislanski, P. T., Williams, K. H., Roberts, J., & Wobber, F. (1997). Estimation of permeable pathways and water content using tomographic radar data. *Leading Edge*, *16*(11), 1623. https://doi.org/10.1190/1.1437539Hunter, J. D. (2007). Matplotlib: A 2D Graphics Environment [Software]. *Computing in Science and Engineering*, *9*(3), 90–95. https://doi.org/10.1109/MCSE.2007.55Irving, J. D., Knoll, M. D., & Knight, R. J. (2007). Improving crosshole radar velocity tomograms: A new approach to incorporating high-angle traveltime data. *Geophysics*, *72*(4), J31–J41. https://doi.org/10.1190/1.2742813Jørgensen, P. R. (1998). DNAPL transport through macroporous, clayey till columns. *Ground Water*, *36*(4), 651–660. https://doi.org/10.1111/j.1745-6584.1998.tb02840.xKeskinen, J., Klotzsche, A., Looms, M. C., Moreau, J., van der Kruk, J., Holliger, K., et al. (2017). Full-waveform inversion of Crosshole GPR data: Implications for porosity estimation in chalk. *Journal of Applied Geophysics*, *140*, 102–116. https://doi.org/10.1016/j.jappgeo.2017.01.001Kessler, T. C., Klint, K. E. S., Nilsson, B., & Bjerg, P. L. (2012). Characterization of sand lenses embedded in tills. *Quaternary Science Reviews*, *53*(C), 55–71. https://doi.org/10.1016/j.quascirev.2012.08.011Kessler, T. C., Comunian, A., Oriani, F., Renard, P., Nilsson, B., Klint, K. E., & Bjerg, P. L. (2013). Modeling fine-scale geological heterogeneity-examples of sand lenses in tills. *Groundwater*, *51*(5), 692–705. https://doi.org/10.1111/j.1745-6584.2012.01015.xKjær, K. H. (1999). Mode of subglacial transport deduced from till properties, Myrdalsjokull, Iceland. *Sedimentary Geology*, *128*(3–4), 271–292. https://doi.org/10.1016/S0037-0738(99)00074-3Kjær, K. H., & Krüger, J. (2001). The final phase of dead-ice moraine development: Processes and sediment architecture, Kötlujökull, Iceland. *Sedimentology*, *48*(5), 935–952. https://doi.org/10.1046/j.1365-3091.2001.00402.xKjær, K. H., Houmark-Nielsen, M., & Richardt, N. (2003). Ice-flow patterns and dispersal of erratics at the southwestern margin of the last Scandinavian Ice Sheet: signature of palaeo-ice streams. *Boreas*, *32*(1), 130–148. https://doi.org/10.1080/03009480310001074Klint, K. E. S., Nilsson, B.,

Troldborg, L., & Jakobsen, P. R. (2013). A poly morphological landform approach for hydrogeological applications in heterogeneous glacial sediments. *Hydrogeology Journal*, *21*(6), 1247–1264. https://doi.org/10.1007/s10040-013-1011-2Klotzsche, A., van der Kruk, J., & Meles, G. A. (2012). Characterizing a low-velocity waveguide using crosshole GPR full-waveform inversion. *14th International Conference on Ground Penetrating Radar (GPR)*, 47–50.Klotzsche, A., Jan van der Kruk, Niklas Linde, Joseph Doetsch, & Harry Vereecken. (2013). 3-D characterization of high-permeability zones in a gravel aquifer using 2-D crosshole GPR full-waveform inversion and waveguide detection. *Geophysical Journal International*, *195*(2), 932–944. https://doi.org/10.1093/gji/ggt275Klotzsche, A., Jonard, F., Looms, M. C., van der Kruk, J., & Huisman, J. A. (2018). Measuring Soil Water Content with Ground Penetrating Radar: A Decade of Progress. *Vadose Zone Journal*, *17*(1), 180052. https://doi.org/10.2136/vzj2018.03.0052Klotzsche, A., Vereecken, H., & Van Der Kruk, J. (2019). Review of crosshole ground-penetrating radar full-waveform inversion of experimental data: Recent developments, challenges, and pitfalls. *Geophysics*, *84*(6), H13–H28. https://doi.org/10.1190/geo2018-0597.1Koyan, P., & Tronicke, J. (2020). 3D modeling of ground-penetrating radar data across a realistic sedimentary model. *Computers and Geosciences*, *137*(January), 104422. https://doi.org/10.1016/j.cageo.2020.104422Lassen, R. N., Sonnenborg, T. O., Jensen, K. H., & Looms, M. C. (2015). Monitoring CO2 gas-phase migration in a shallow sand aquifer using cross-borehole ground penetrating radar. *International Journal of Greenhouse Gas Control*, *37*, 287–298. https://doi.org/10.1016/j.ijggc.2015.03.030Liu, L., Lane, J. W., & Quan, Y. (1998). Radar attenuation tomography using the centroid frequency downshift method. *Journal of Applied Geophysics*, *40*(1–3), 105–116. https://doi.org/10.1016/S0926-9851(98)00024-XLooms, M. C., Jensen, K. H., Binley, A., & Nielsen, L. (2008). Monitoring Unsaturated Flow and Transport Using Cross-Borehole Geophysical Methods. *Vadose Zone Journal*, *7*(1), 227–237. https://doi.org/10.2136/vzj2006.0129Looms, M. C., Klotzsche, A., van der Kruk, J., Larsen, T. H., Edsen, A., Tuxen, N., et al. (2018). Mapping sand layers in clayey till using crosshole ground-penetrating radar. *Geophysics*, *83*(1), A21–A26. https://doi.org/10.1190/geo2017-0297.1McCabe, A. M. (1987). Quaternary deposits and glacial stratigraphy in Ireland. *Quaternary Science Reviews*, *6*(3–4), 259–299. https://doi.org/10.1016/0277-3791(87)90008-4McKinney, W. (2010). Data Structures for Statistical Computing in Python [Software]. *Proceedings of the 9th Python in Science Conference*, *1*(Scipy), 56–61. https://doi.org/10.25080/majora-92bf1922-00avan der Meer, J. J. M., & Menzies, J. (2011). The micromorphology of unconsolidated sediments. *Sedimentary Geology*, *238*(3–4), 213–232. https://doi.org/10.1016/j.sedgeo.2011.04.013Molyneux, J. B., & Schmitt, D. R. (1999). First-break timing: Arrival onset times by direct correlation. *Geophysics*, *64*(5), 1492–1501. https://doi.org/10.1190/1.1444653Nielsen, L., Looms, M. C., Hansen, T. M., Cordua, K. S., & Stemmerik, L. (2010). Estimation of Chalk Heterogeneity from Stochastic Modeling Conditioned by Crosshole GPR Traveltimes and Log Data. In *Advances in Near-Surface Seis-*

mology and Ground-penetrating Radar (pp. 379–396).Nilsson, B., Sidle, R. C., Klint, K. E., Bøggild, C. E., & Broholm, K. (2001). Mass transport and scale-dependent hydraulic tests in a heterogeneous glacial till - Sandy aquifer system. *Journal of Hydrology*, *243*(3–4), 162–179. https://doi.org/10.1016/S0022-1694(00)00416-9Oberröhrmann, M., Klotzsche, A., Vereecken, H., & Van Der Kruk, J. (2013). Optimization of acquisition setup for cross-hole GPR full-waveform inversion using checkerboard analysis. *Near Surface Geophysics*, *11*(2), 197–209. https://doi.org/10.3997/1873-0604.2012045Peterson, Jr., J. E. (2001). Pre-inversion Corrections and Analysis of Radar Tomographic Data. *Journal of Environmental and Engineering Geophysics*, *6*(1), 1–18. https://doi.org/10.4133/JEEG6.1.1Selsing, L. (1980). Dødisomradet ved Brorfelde, Nordvest-Sjælland. *Dansk Geologisk Forening Årskrift for 1979*, 85–97.Shaw, J. (1987). Glacial sedimentary processes and environmental reconstruction based on lithofacies. *Sedimentology*, *34*(1), 103–116. https://doi.org/10.1111/j.1365-3091.1987.tb00563.xSidle, R. C., Nilsson, B., Hansen, M., & Fredericia, J. (1998). Spatially varying hydraulic and solute transport characteristics of a fractured till determined by field tracer tests, Funen, Denmark. *Water Resources Research*, *34*(10), 2515–2527. https://doi.org/10.1029/98WR01735Slob, E., Sato, M., & Olhoeft, G. (2010). Surface and borehole ground-penetrating-radar developments. *Geophysics*, *75*(5). https://doi.org/10.1190/1.3480619Svendsen, E. B., Nielsen, L., Nilsson, B., Kjær, K. H., & Looms, M. C. (2020). Data-driven source wavelets for cross-hole ground-penetrating radar full-waveform modeling. In *18th International Conference on Ground Penetrating Radar* (pp. 392–395). Golden, Colorado: Society of Exploration Geophysicists. https://doi.org/10.1190/gpr2020-102.1Tarantola, A. (2005). *Inverse Problem Theory and Methods for Model Parameter Estimation*. SIAM.The pandas development team. (2020). pandas [Software]. Zenodo. https://doi.org/10.5281/zenodo.3509134Virtanen, P., Gommers, R., Oliphant, T. E., Haberland, M., Reddy, T., Cournapeau, D., et al. (2020). SciPy 1.0: fundamental algorithms for scientific computing in Python [Software]. *Nature Methods*, *17*(3), 261–272. https://doi.org/10.1038/s41592-019-0686-2Warren, C., Giannopoulos, A., & Giannakis, I. (2016). gprMax : Open source software to simulate electromagnetic wave propagation for Ground Penetrating Radar. *Computer Physics Communications*, *209*, 163–170. https://doi.org/10.1016/j.cpc.2016.08.020Waskom, M. (2021). seaborn: statistical data visualization [Software]. *Journal of Open Source Software*, *6*(60), 3021. https://doi.org/10.21105/joss.03021 Wunderlich, T., & Rabbel, W. (2013). Absorption and frequency shift of GPR signals in sandy and silty soils: Empirical relations between quality factor Q, complex permittivity and clay and water contents. *Near Surface Geophysics*, *11*(2), 117–127. https://doi.org/10.3997/1873-0604.2012025Yilmaz, Ö. (2001). *Seismic data analysis: Processing, inversion , and interpretation of seismic data*. Tulsa: Society of Exploration Geophysicists.Zhou, B., & Fullagar, P. K. (2001). Delineation of sulphide ore-zones by borehole radar tomography at Hellyer Mine, Australia. *Journal of Applied Geophysics*, *47*(3–4), 261–269. https://doi.org/10.1016/S0926-9851(01)00070-2Zhou, Z., Klotzsche, A., Her-

mans, T., Nguyen, F., Schmäck, J., Haruzi, P., et al. (2020). 3D aquifer characterization of the Hermalle-sous-Argenteau test site using crosshole ground-penetrating radar amplitude analysis and full-waveform inversion. *Geophysics*, *85*(6), H133–H148. https://doi.org/10.1190/geo2020-0067.1